Article:

Oliveira, N.M., Fostera, K.R. and Durham, W.M. (2016) Single-cell twitching chemotaxis in developing biofilms. Proceedings of the National Academy of Sciences , 113 (23). pp. 6532-6537. ISSN 0027-8424

https://doi.org/10.1073/pnas.1600760113

Single-cell twitching chemotaxis in developing biofilms

Supplementary Information

We present below a detailed description of our microfluidic experiments and respective quantitative analyses, along with our supplementary figures and descriptions of supplementary movies.

Materials and Methods

Subsurface twitching assay

We followed standard protocols previously described (1, 2). Briefly, strains were grown overnight in LB (37°C, 250 rpm) from frozen stocks and spotted on 1.5% LB agar, which were incubated at 37°C under static conditions for 24 hours. Using cells isolated from a single colony, we stab-inoculated Petri dishes filled with 1% agar (LB or TB) to deposit bacteria at the interface between the agar and the underlying plastic dish. After 48 hours of incubation at 37°C the dishes were photographed with a DSLR camera (EOS 30D, Canon). The software Fiji (3) was used to enhance the contrast (over the whole image) to make the relatively faint twitching rings on the bottom of the plate more visible.

Microfluidic experiments

Two different microfluidic setups were used in this study. We used the commercially available Bioflux 200 system (Fluxion Biosciences) for all microfluidic experiments except the alternating gradient experiments presented in Fig. 4D-G and Figs. S12, S13, S14, which used a custom designed microfluidic device (Fig. S11). Briefly, microfluidic channels were primed with tryptone broth (TB) medium as previously described (4). Exponential phase cells were then introduced and allowed to attach to the surface for 20 min in the absence of flow. Planktonic and weakly adhered cells were then flushed from the test section by applying a flow rate of 40 μl h^{-1} for 10 min. The flow rate was then reduced to 4 μl h^{-1} at $t = 0$, which was maintained for the reminder of the experiment. Cells were imaged at a rate of 1 frame min^{-1}, with the exception of the Δ*pilH* (Fig. 3) and Δ*flgK* mutants (Fig. S5), which, due to their very fast motility, were imaged at 13 frames min^{-1} and 15 frames min^{-1} respectively. All microfluidic experiments were conducted at 22°C. We imaged microfluidic experiments using a Zeiss Axio Observer inverted microscope with a Zeiss 20X Plan Apochromat objective, Zeiss AxioCam MRm camera, and a Zeiss Definite Focus system. Fluorescent cells were imaged using either a Zeiss LSM 700 scanning laser confocal system (Fig. 1G) or with a Zeiss HXP 120C light source (Fig. 1F, Fig. S1).

Experiments using Bioflux microfluidic devices

The test sections of all Bioflux channels were 350 μm wide and 75 μm deep, but they came in two slightly different designs (Fig. S2). Studies with fluorescein dye showed the different geometries of these designs upstream of the test section caused them to generate slightly different chemical distributions (Fig. S2A,D). We accounted for these differences in the model of diffusion that simulates the distribution of chemoattractant in these devices (see Fig. S2B,C,E,F, and section below).

The experiments in Fig. 2 were conducted using the Bioflux "Invasion" channels (Fig. S2). To continuously track the location of the chemoattractant in these experiments, we mixed the solution containing DMSO or succinate with Chicago Sky Blue 6B dye (3% by volume of saturated stock solution, Sigma Aldrich). Both dye and cells were visualized simultaneously within the same image. We confirmed in a separate experiment that the dye did not induce a chemotactic response (Fig. S15). Every 3 hours we reversed the direction of the chemoattractant gradient by manually replacing the fluid in the reservoirs that were connected to each inlet. While this process took approximately five minutes, it required that the microfluidic system be removed from the microscope and thus it was not possible to continuously image cells as the chemoattractant gradient changed direction. Thus, to quantify reversals in cells responding to a change in the chemoattraction direction (Fig. 4D,E,F,G) required the development of a custom microfluidic device (Fig. S11) that did not have this limitation.

Alternating gradient experiment using custom microfluidic device

To observe cells as they respond to a chemoattractant gradient that alternates in direction, we designed a microfluidic device with four inlet ports (Fig. S11). Molds with this design were fabricated from SU-8 on a silicon wafer (FlowJEM, Toronto, Canada). Microfluidic channels were cast using PDMS (Sylgard 184, Dow Corning) and holes for tubing were punched using a Harris Unicore 1.5 mm biopsy tool (Agar Scientific). Cured PDMS was bonded to glass coverslips (50 mm by 75 mm, No. 1 thickness, Agar Scientific) with a corona treater (BD-20AC, Electro-Technic Products) using previously described techniques (5). Tygon microbore tubing (0.06

inch outside diameter) was used to plumb both the inlets and outlets of the device. The outlet was connected to a single 10 ml syringe (Becton Dickinson) mounted on a syringe pump (PhD Ultra, Harvard Apparatus) that generated flow through the device via suction. The test section of the device is 600 μm wide and 75 μm deep.

After the system was primed with TB, exponential phase cells (WT or Δ*pilG*) were drawn into the device at 100 μl min^{-1} using the pair of inlets marked 'A' in Fig. S11. After cells reached the test section, tubes connected to all four inlets were clamped with hemostats for 20 mins to allow cells to attach to surfaces in the absence of flow. Next, the tubing connected to the inlets were inserted to reservoirs containing either TB or 350 mM DMSO and Chicago Sky Blue 6B dye dissolved in TB. We then pulled fluid through the device at 100 μl min^{-1} to both remove planktonic cells and allow the chemoattractant to reach test section of the device. The flow was then reduced to 5 μl min^{-1} for the remainder of the experiment. We then clamped the tubes connected to one pair of inlets, which exposed cells to a DMSO gradient. Next, we changed the direction of the gradient approximately every eight minutes by sequentially unclamping and clamping the tubes connected to the inlets marked 'A' and 'B' in Fig. S11. Our analysis began at t = 0, when we first changed the direction of the gradient. Dye and cells were imaged simultaneously every four seconds at x = 2.5 mm (Fig. S11). While the distribution of dye was analyzed in each frame, cells were tracked in every other frame (i.e. every eight seconds) owing to computational constraints.

Preliminary experiments showed that the vast majority of correct reversals occurred within eight minutes of the gradient changing direction (Fig. 4G, white bars). Since the total duration of experiments is limited by cell crowding, we reversed the gradient every eight minutes to generate as many reversals as possible before the surface became densely covered with cells and the tracking of individuals became difficult.

Characterization of concentration field in Bioflux devices using fluorescein and mathematical modeling

The distribution of chemoattractant, C, within the Bioflux devices was mapped using fluorescein, a fluorescent dye whose diffusion coefficient, D, approximates that of the low molecular weight compounds used in this study. Fluorescein was observed to strongly affect cell growth, so we conducted separate experiments without cells to resolve the distribution of C and mapped this back onto experiments with cells.

Imaging was conducted using the microscopy setup noted above except with a Zeiss EC Plan Neofluar 10X objective, a Zeiss LSM 700 scanning laser confocal unit to measure fluorescent intensity, and a Zeiss LSM T-PMT unit to simultaneously visualize the channel geometry. We recorded z-stacks of images at multiple, overlapping positions along the length of the device and the maximum fluorescent intensity in z was used to obtain the relative fluorescein concentration at each x,y position. Slight variations in C occurred along x because thermally induced fluctuations in z led to differences in the maximum measured fluorescent intensity between adjacent images (Fig. S2A,D).

To correlate cell movement with the chemoattractant distribution we used a mathematical model to calculate C within the Bioflux devices. More specifically, we used a one dimensional, time dependent diffusion equation to simulate molecular diffusion in the y direction and then used the mean flow velocity in the device to transform time into distance along x. We consider a one-dimensional domain with impermeable, no-flux boundaries at $y = -L/2$ and $y = L/2$. At $t = 0$ two regions of constant concentration are initialized: $C = C_{\mathrm{MAX}}$ in the region $-L/2 < y < h - L/2$ and $C = 0$ in the region $h - L/2 < y < L/2$. Subject to these initial and boundary conditions, the solution of the one dimensional diffusion equation is given by (6):

$$C = C_{MAX}\left\{\frac{h}{L} + \frac{2}{\pi}\sum_{n=1}^{\infty}\frac{1}{n}\sin\frac{n\pi h}{L}\exp(-Dn^2\pi^2t/L^2)\cos\frac{n\pi(y+L/2)}{L}\right\}.$$

This time dependent solution was transformed, assuming constant advection speed, to distance along the device via the substitution $t = x\,U^{-1}$, where $U = 42$ µm s^{-1} is the mean flow velocity, $L = 350$ µm is the channel width, and $D = 10^2$ µm^2 s^{-1}. This approach assumes uniform flow and that the distribution of chemoattractant is constant over the depth of the device. For modeling the Bioflux “Invasion” plates, which are symmetric about $y = 0$, we used $h = L/2 = 175$ µm, which yielded a distribution of C that closely matched that obtained experimentally using fluorescein dye (Fig. S2D,E,F).

For modelling the Bioflux “WPM” plates, which have a slight asymmetry upstream of the test section, we used $h = 160$ µm and introduced an offset in y to directly match position of the $C = 0.5$ isocontour in the fluorescein experiment (Fig. S2A,B,C). This concentration field was used exclusively for presentation purposes (Fig. 1B), but not for any quantitative analyses.

Modeling the chemical environment in the alternating gradient experiment

In the alternating gradient experiment, we used a larger flow velocity

(U = 1.85 mm s^{-1}) to minimize the variation in chemical stimuli along the x direction of the device. The characteristic width of the gradient generated by diffusion can be approximated as $L \approx \sqrt{2Dx/U}$ and we imaged at x = 2.5 mm (Fig. S11), yielding $L \approx$ 20 – 50 μm for D = 10^2 –10^3 μm^2 s^{-1}, which is in the range experimentally observed with the dye (Fig. 4D). Our field of view spans 0.45 mm in the x dimension: the formula above predicts that the width of the gradient increases by ≈10% from the upstream to the downstream edge of our field of view. Thus, within our field of view, cells at the same y position experience nearly the same chemical environment regardless of their position in x. This small amount of variation allows us to average C along x to present its spatiotemporal variation as a kymograph (Fig. 4D,E) and pool cell behaviour along x (Fig. 4F,G).

Cell tracking

All images were processed using the open source software Fiji (3) and its associated plugins. After correcting the time series of images for thermally-induced drift of the microscope stage (using the Image Stabilizer plug in) and enhancing the contrast of cells (using background subtraction and noise reduction functions), we tracked the movement of cells through space and time using the TrackMate plug in (7). To distinguish solitary cells from those residing within groups, we calculated the mean image intensity within a 3 μm radius from the centroid each detected cell. Cells in close proximity to other cells (e.g. those within a cluster) yielded larger mean intensities than solitary cells, which allowed us to exclude the former prior to running the tracking algorithm. To quantify cell length and cell orientation we fitted each cell with an ellipse at every time point, functionality that is accessible by running

Trackmate via a Jython script (this feature is not available in the Graphical User Interface). All tracking data was exported from Fiji to Matlab (Mathworks) for subsequent analysis.

Experiments where dye gradients and cells were visualized simultaneously within the same image (Figs. 2, 4D-G, and Figs. S12, S13, S14, S15) required additional processing. To isolate cells, we removed the variable intensity background by normalizing the local contrast with Fiji's Integral Image Filter plugin. To isolate the dye, we removed cells from the image using Fiji's Rolling Ball Background Subtraction function.

Analysis of cell behavior

Calculation of chemotactic bias

The strength of the chemotactic response, β, was quantified by dividing number of cells moving up the gradient by the number of cells moving down the gradient as a function of time. While analogous metrics have been used to quantify chemotaxis in swimming bacteria (8), twitching cells exhibit jerky, unsteady movement (9), such that the instantaneous direction of a cell's movement is not representative of the direction of its transport over longer timescales. Thus, in our calculation of β we defined the direction of movement using a cell's net displacement over the length of its trajectory (with the exception of Fig. 2, see below). In addition, we excluded non-motile cells and cells that do not exhibit appreciable movement from their origin. This was accomplished by calculating the net to gross displacement ratio (NGDR), which is defined as the straight line distance between the start and end points of a trajectory divided by the total distance travelled along the path of the trajectory (10). Trajectories with NGDR<0.15 were excluded from our calculation. This threshold was chosen based on visual inspection to exclude cells with convoluted paths that do not show significant movement in any direction (trajectories with NGDR<0.15 are shown in Movie S1). All measurements of β were obtained by analyzing cells within in two adjacent fields view of the microscope (with the exception of Fig. 2, see below), which spanned the full channel width in y and approximately from $x = -0.05$ to 0.85 mm.

The rose plots in Fig. 1B,C were obtained by calculating the angle, θ, from each trajectory's from origin to its terminus. The resulting angles were weighted by the trajectory length, binned within 12 equally spaced bins around the unit circle, and normalized to obtain the probability density function. As cell crowding significantly restricted cell movement at later time points, this analysis considered only trajectories collected from $t = 0$ to 5 h.

In Fig. 2, we quantified how cells react to changes in the direction of the gradient. To capture changes in motility that occur mid-trajectory, we subdivided trajectories into segments 16 minutes long and used these to calculate $\bar{\theta}$ (Fig. 2G) and β (Fig. 2H). This segment length is long enough to capture the overall direction of cell movement (smoothing over the frequent, rapid changes in movement direction that are characteristic of twitching motility), whilst being short enough capture the response of cells to the changing gradient with reasonable temporal resolution (Fig. 2G). The normalized gradient, G, at each point along the trajectory was calculated via bilinear interpolation from the mathematical model of diffusion (Fig. S2F) and was averaged to obtain the mean G for each segment. In these experiments cells were imaged in only one field of view, which spanned the full channel width in z and approximately from $x = -0.05$ to 0.43 mm.

Calculation of the apparent aspect ratio

To quantify the orientation of cells relative to the surface, we calculated cell length divided by the cell width to obtain its aspect ratio as viewed from below the surface (within an approximately 1 μm depth of field along z). *P. aeruginosa* cells have a elongated cylindrical shape, such that when cells are oriented perpendicular to the surface they have an apparent aspect ratio of one, whereas cells oriented parallel to the surface yield an aspect ratio greater than one. The apparent aspect ratio of each cell was calculated over time and data from all trajectories were pooled to obtain the probability density function for each strain (Figs. S5B, S8).

Calculation of root mean squared displacement

The root mean square displacement (RMSD) measures how far cells venture from their initial position as a function of time, allowing us to objectively compare motility of between different strains (Fig. 3C) and in different chemical environments (Fig. S4). The RMSD is given by

$$RMSD(\tau) = \sqrt{\langle (x(\tau) - x_O)^2 + (y(\tau) - y_O)^2 \rangle},$$

where τ is the time lag, $[x_o, y_o]$ is a cell's initial position, and angled brackets denote averaging. When plotted on a log-log plot (Fig. S4B), the RMSD(τ) of twitching cells exhibits a slope of approximately one for small τ, denoting ballistic motion, and transitions into a slope of approximately ½ for larger τ, which corresponds to diffusive motion. Similar observations have been made for the motility of a diverse range of microorganisms (11).

Reversal detection

While the reversals in *M. xanthus* have been comprehensively studied (12), reversals in twitching *P. aeruginosa* have largely escaped mention in the literature (see Semmler et al 1999 (2) for an exception). One possible reason for this is that the latter occur much more infrequently: while *M. xanthus* cells reverse once every several minutes (13, 14), we find that on average *P. aeruginosa* cells reverse once every few hours (Fig. 4C). Reversals in *M. xanthus* are typically enumerated manually by direct observation (13, 14), but quantifying the relatively infrequent reversals exhibited by *P. aeruginosa*, necessitated the development of an automated algorithm to detect reversal events among a large number of cell trajectories.

Cells tend to move along their long axis (Fig. S9) by pulling themselves along using pili that tend extend from their leading pole (15, 16). A reversal occurs when a cell stops and moves back in the other direction without turning. Under idealized conditions then a reversal occurs when a cell's body orientation, ϕ, remains constant, but its movement direction, θ, changes by $\pm\pi$ such that the leading pole becomes its trailing pole (Fig. S9). However, in practice both the unsteady, jerky movement of twitching motility and cell division (Fig. 4A, B) can generate events that a basic algorithm would misdiagnose as a reversal. Since 'true' reversals are readily observed by eye (Movies S3, S4, S5, S6), our approach was to develop an algorithm that agrees with what one would obtain by direct observation. To achieve this, we developed a system of filters to discriminate true reversals from spurious events and adjusted parameters of these filters using direct observation as a benchmark. Importantly, we used exactly the same method to analyse each experiment, allowing us to objectively compare the reversal rate in different strains and in different chemical environments.

To detect reversals in the static gradients, we first smoothed trajectories using a 10 min moving average filter (Fig. 4A) to calculate the mean movement direction, θ_M. At each time point along the trajectory we identify the leading pole by determining which of the cell's two poles is most closely aligned with the direction of cell movement (i.e. we determine whether ϕ or $\phi+\pi$ forms the smallest angle with θ_M). A potential reversal occurs when a cell's leading pole shifts to the opposite side of the cell between subsequent time points.

We used the same procedure to identify potential reversals in the alternating gradient experiments, but because reversals were induced more frequently and cells were tracked at a higher temporal resolution (every 8 seconds, as opposed to every minute in the static gradient experiments) we used a 160 second moving average filter to obtain θ_M.

After identifying potential reversals, we developed a series of filters to objectively resolve which of these are 'true' reversals and which result from aberrant cell motion. Below we describe each of these filters and the specific cell behaviour that they are designed to discriminate. Smoothed cell trajectories were used in each of these calculations.

We exclude potential reversals from:

1. Cells who are sliding sideways, for example, when they are pushed by flow. These cells have motility that is not aligned with the cell's long axis before and after the reversal. We measure the cosine of the angle between the direction of the leading pole and the direction of cell motility and reversals are excluded if this is smaller than 0.55.
2. Cells who are upright and only attached by one pole to the surface (whose mean apparent aspect ratio is smaller than 1.4 either before or after the reversal).
3. Cells who are non-motile (speed is smaller than 0.08 μm min^{-1} either before or after the reversal).
4. Cells who are rapidly pivoting about their point of attachment with the surface (whose bodies rotate more than $\pi/8$ radians between subsequent time points).
5. Cells that are jiggling back and forth on the surface. We do this by excluding cells that have experienced another potential reversal in the preceding or following 5 min in the static gradient experiments (2.4 min in the alternating gradient experiments).
6. Cells undergoing division. Cell division events were detected by measuring the change in cell length over time. We exclude potential reversals in trajectories that experience a large reduction in cell length immediately before or after a reversal. Apparent reversals arising from cell division are marked in Movies S3 and S4.

Calculation of reversal rate

To estimate the reversal rate, we divided the total number of reversals in an experiment by the cumulative time of all trajectories. In the calculation of the latter, we omitted the trajectories of weakly motile cells that are incapable of generating reversals (owing to our specification of a minimum cell speed, see previous section). This ensures consistency when comparing the reversal rate across experiments that may have different fractions of weakly motile cells.

In experiments with a static DMSO gradient (Fig. 4C) we separately measured the reversal rate of cells that are initially traveling down the gradient (white bars) and cells initially traveling up the gradient (black bars). The rate of 'correct' reversals was calculated by dividing the total number of correct reversals by the cumulative time that trajectories moved down the gradient. Conversely, the rate of 'incorrect' reversals was calculated by dividing the total number of incorrect reversals by the cumulative time that trajectories moved up the gradient. In both calculations, the cumulative time was adjusted using the cell speed consideration noted in the previous paragraph.

SI Figures

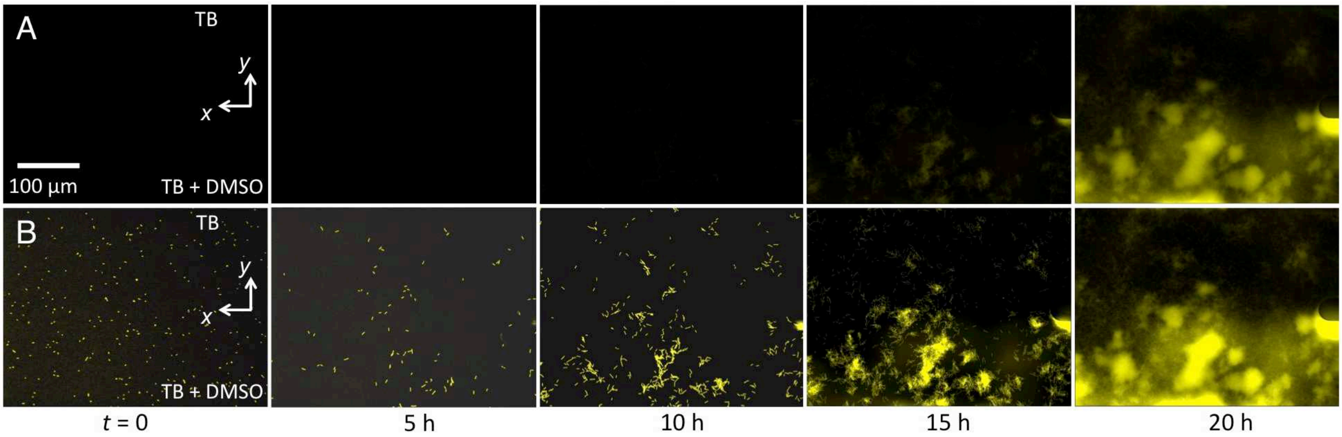

Figure S1: Quantifying the dynamics of biofilm formation using epifluorescent microscopy. (A, B) To illustrate how biofilms formed in our devices over time, we imaged cells that constitutively produce yellow fluorescent protein every two minutes to generate the kymograph shown in Fig. 1F. Shown here are five of the 600 epiflourescent images from this time series. Raw images are shown in (A), whilst each of the images shown in (B) has had the contrast adjusted such that the relatively weak signal from single cells is visible at early time points. At the beginning of the experiment cells are allowed to attach to the surface under quiescent conditions and then at $t = 0$ the flow used to generate the DMSO gradient is turned on (SI Materials and Methods). This flow detaches a fraction of the cells, so that there are fewer surface attached cells at $t = 5$ h. However, cell division leads to the formation of microcolonies by $t = 15$ h and by $t = 20$ h the biofilms are ≈20 µm thick (Fig. 1G).

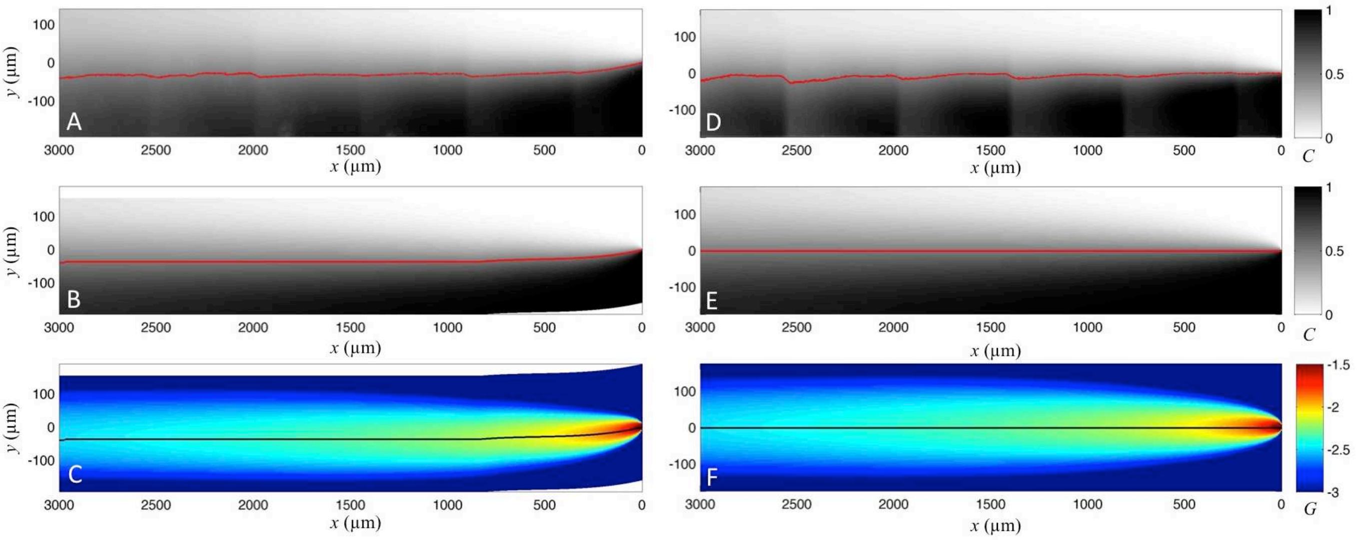

Fig. S2: A mathematical model accurately predicts the distribution of chemoattractant in two Bioflux microfluidic devices. The "WPM" channels (**A**, **B**, **C**) and "Invasion" channels (**D**, **E**, **F**) generate slightly different chemoattractant distributions owing to the different geometry of their inlets. In experiments without bacteria, we measured the normalized concentration, *C*, of fluorescein in each channel design using confocal microscopy (A, D, Supplementary Methods). This distribution was simulated using an analytical model of molecular diffusion (B, E), which was then differentiated to obtain, *G*, the normalized chemoattractant gradient (C, F, Supplementary Methods). The $C = 0.5$ contour is marked with red line in the upper two rows and a black line in the lower row. The WPM channels generate a chemoattractant distribution slightly asymmetric about $y = 0$, which was accounted for in the model by matching the $C = 0.5$ contour from the empirical measurement (red line in A, SI Materials and Methods). Note the different scales in *x* and *y*.

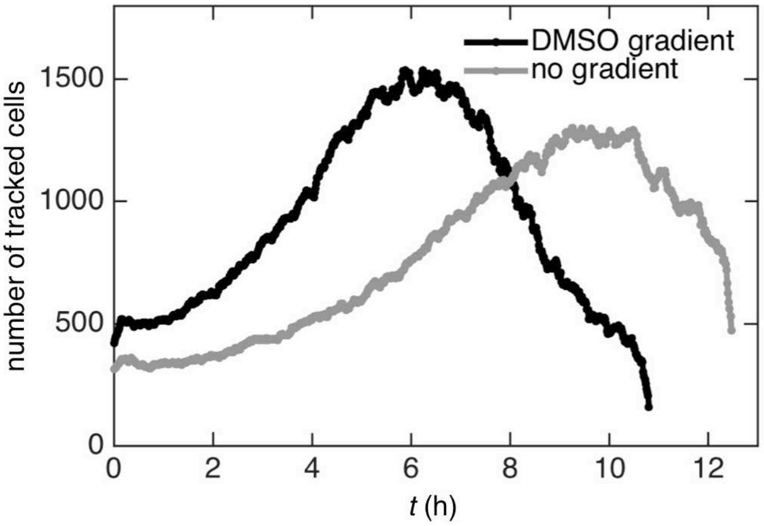

Fig. S3: Automated cell tracking allows us to measure the aggregate behaviour of a large number of cells. Here we plot the number of cells tracked within each frame of the experiments shown in Fig. 1. The number of cells initially increases as a result of cell division, but then decreases as cells crowd the surface such that individual cells can no longer be discerned (Movie S1). The analyses shown in Fig. 1D,E are derived from the trajectories of this large population of cells. The analyses shown elsewhere in this paper are derived from a similar number of cells.

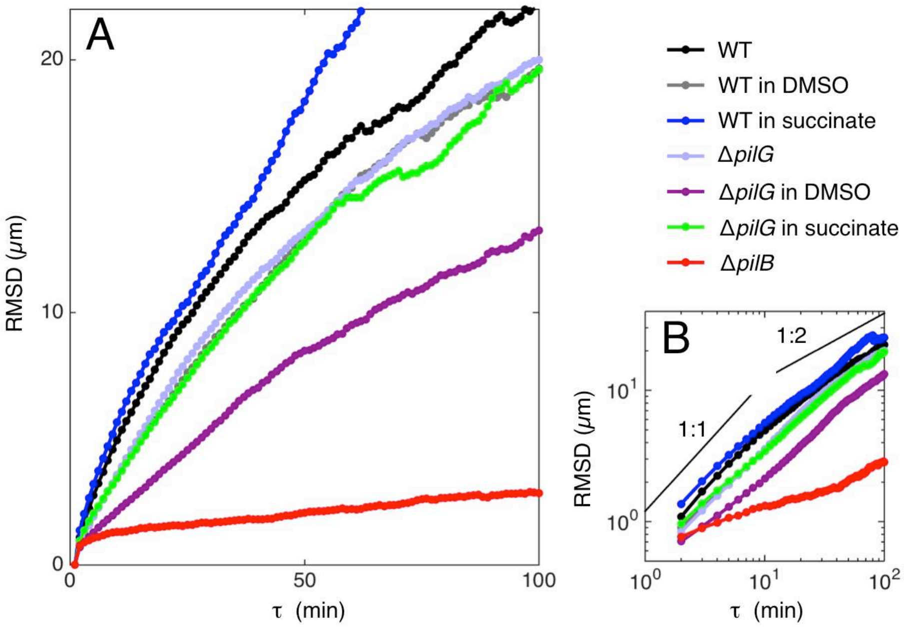

Fig. S4: Wild-type and Δ*pilG* cells exhibit reduced motility in the presence of DMSO, but not in the presence of succinate. Measurements of the root mean square displacement, *RMSD*, reveals that in DMSO cells venture a shorter distance from their origin over a time lag, τ. However, in succinate wild-type cells exhibit a larger *RMSD* than in the control, whilst the motility of Δ*pilG* cells is largely unaffected by succinate. Data for the nonmotile Δ*pilB* strain is shown for comparison. Here the *RMSD* is plotted as function of τ on linear (**A**) and logarithmic (**B**) axes. The line with a 1:1 slope in (B) corresponds to ballistic movement, whilst the 1:2 slope corresponds to diffusive movement. All experiments were performed in the absence of gradients in either pure TB, TB supplemented with 350 mM DMSO, or TB supplemented with 2 mM succinate.

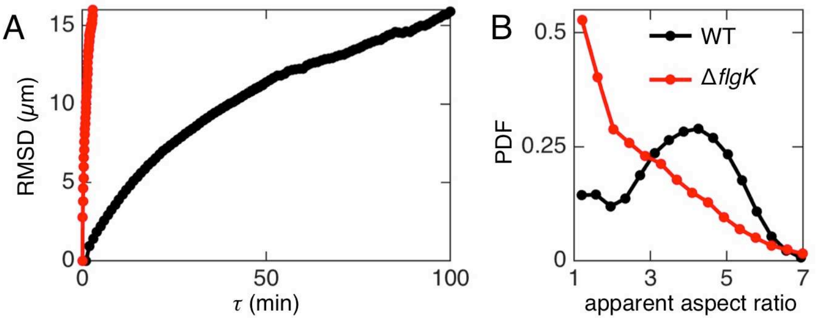

Fig. S5: Cells lacking flagella perform twitching motility and tend to stand upright on the surface. (**A**) The root mean squared displacement of Δ*flgK* cells is larger than that of wild-type cells at the same time lag τ, which means that flagellum-null cells move even faster than the wild-type. (**B**) Δ*flgK* cells tend to move with their long axis perpendicular to the surface such that their apparent aspect ratio (the cell length divided by cell width, as viewed from below the surface, SI Materials and Methods) is strongly peaked at unity, as we found for Δ*pilH* cells (Fig. S8). In comparison, wild-type cells orient themselves parallel to the surface such that their apparent aspect ratio peaks at ≈ 4. These findings are in agreement with a previous study that also found cells lacking flagella have enhanced motility and increased propensity to stand upright (17).

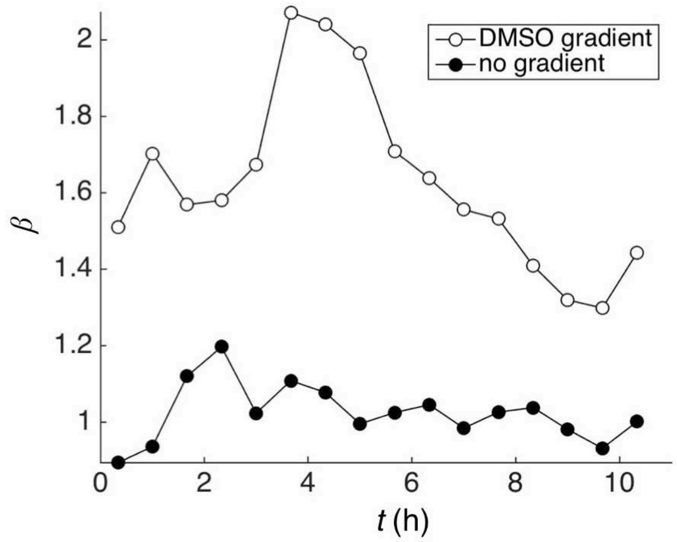

Fig. S6: The response regulator CheY1, which mediates chemotaxis in swimming *P. aeruginosa* cells (18-20), is not required for twitching chemotaxis. *cheY1*-null cells exposed to a gradient of DMSO (line with white circles) exhibit a chemotactic bias, β, much larger than they exhibit in the absence of chemical gradients (line with black circles), indicating that they are strongly chemotactic.

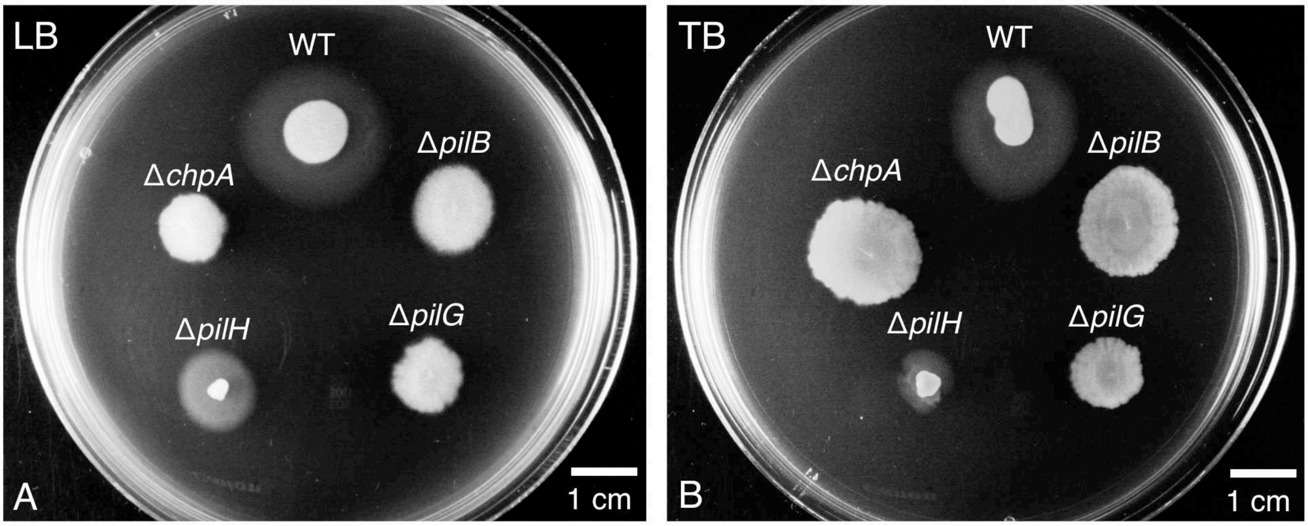

Fig. S7: The behaviour of Chp chemosensory mutants in agar-based 'stab' assays. Twitching motility in this assay is detected by the formation of the so-called *twitching rings* (faint rings that form around colonies), which form at the bottom of plates, between the plastic and the agar. In-frame deletions of *pilB*, *chpA* and *pilG* prevent twitching rings while *pilH*-null cells form smaller twitching rings than the respective WT. We recapitulate the data published previously using plates containing Luria broth (LB, **A**) (1, 21) and also study twitching motility in plates containing tryptone broth (TB, **B**) as this is the growth medium used in our microfluidic experiments. Plates were imaged after 48 hours of incubation.

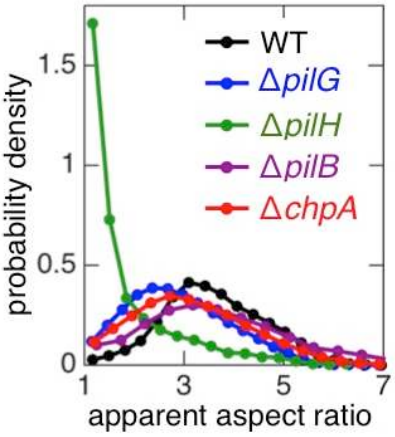

Fig. S8: Cells lacking PilH tend to move with their long axis perpendicular to the surface, leading to an apparent aspect ratio of ≈1, whereas wild type cells and remainder of the Chp mutants we tested orient themselves parallel to the surface such that their apparent aspect ratio is >1. Here the apparent aspect ratio is the cell length divided by cell width, as viewed from below the surface (SI Materials and Methods).

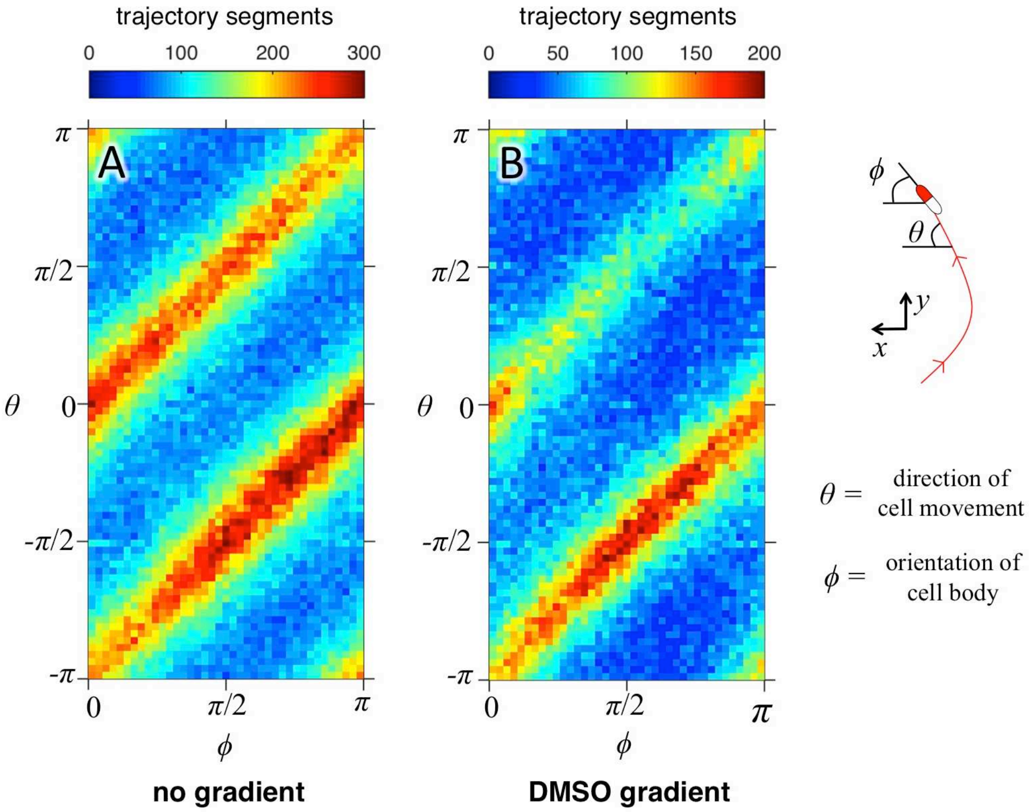

Fig. S9: Twitching cells tend to move along their long axis both the absence (A) and presence (B) of a DMSO gradient. The orientation of the cell body, ϕ, and the direction of cell motility, θ, were calculated at each time point along the trajectories (SI Materials and Methods). Each pair of angles was used to generate a histogram that shows their relative frequency in ϕ - θ space. While the orientation of a cell body, which lacks polarity, can be fully specified by its angle in the half plane, $\phi = [0, \pi]$, cell motility can occur in any direction on the unit circle, $\theta = [-\pi, \pi]$. When a cell undergoes a “reversal”, ϕ remains constant, but θ shifts by $\pm\pi$. Strong clustering in (A) along the lines $\phi = \theta$ and $\phi = \theta - \pi$ reveals that in the absence of a gradient cells tend to move along their long axis, likely owing to fact that the pili, with which cells pull themselves along a surfaces, cluster at their poles (15, 16). A similar distribution is observed in a gradient of DMSO (B), but cells preferentially move along their long axis in the direction of increasing DMSO concentration.

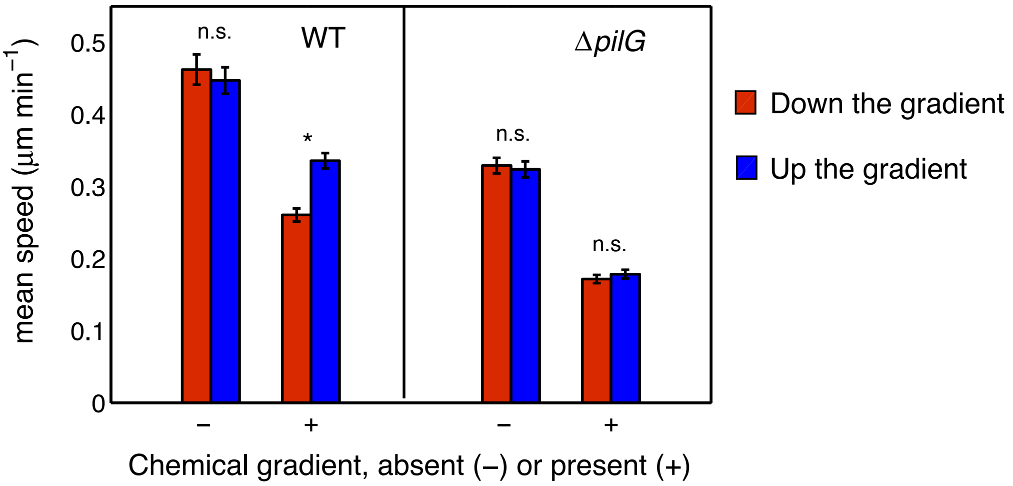

Fig. S10: Wild-type cells traveling towards the DMSO source ("up the gradient") move approximately 25% faster than cells moving away from the DMSO source ("down the gradient"), but this asymmetry in speed is absent in Δ*pilG* cells and in gradient-free controls. (+) denotes data from experiments with a DMSO gradient, whereas (−) denotes data from control experiments which use pure tryptone broth (TB). For each experiment, we smoothed trajectories with a 10 min moving average filter and calculated the speed and direction of cell movement at each point along these smoothed trajectories. The resultant measurements of cell speed were pooled by whether they were recorded as the cell moved in the $-y$ or $+y$ direction, which correlates to "Up the gradient" and "Down the gradient" respectively. In the gradient-free controls, "Up the gradient" and "Down the gradient" correspond to cell speed in the same y direction as experiments with a DMSO gradient (Fig. 1). "n.s." denote non-significant differences in speed while "*" denote a p-value < 0.05, according to Wilcoxon rank tests at a significance of 5%. Error bars are standard errors of means. We note that the overall reduction in cell speed observed in experiments with DMSO is consistent with the observation that DMSO tends to reduce cell motility (Fig. S4).

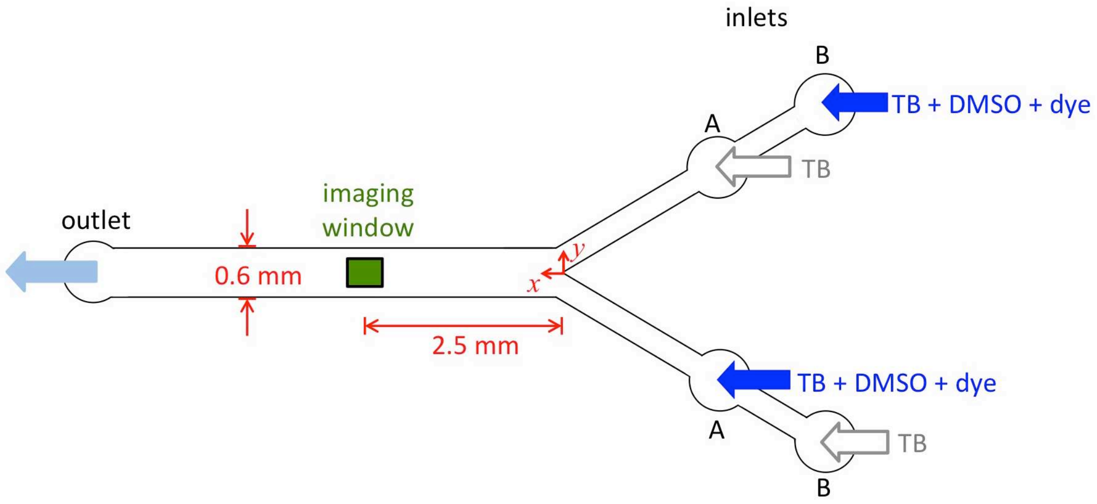

Fig. S11: A schematic of the microfluidic device used to rapidly alternate the direction of a chemoattractant gradient. The four inlets of the device were connected to reservoirs containing either TB mixed with DMSO and Chicago Blue dye or pure TB. Fluid was continuously withdrawn from the outlet and the pairs of inlets marked ‘A’ and ‘B’ were sequentially clamped (SI Materials and Methods) such that fluid is pulled from only one pair of inlets at a time. Moving the clamps to the opposite pair changes the direction of the chemoattractant gradient in the imaging window (green box). The channel is 75 µm deep.

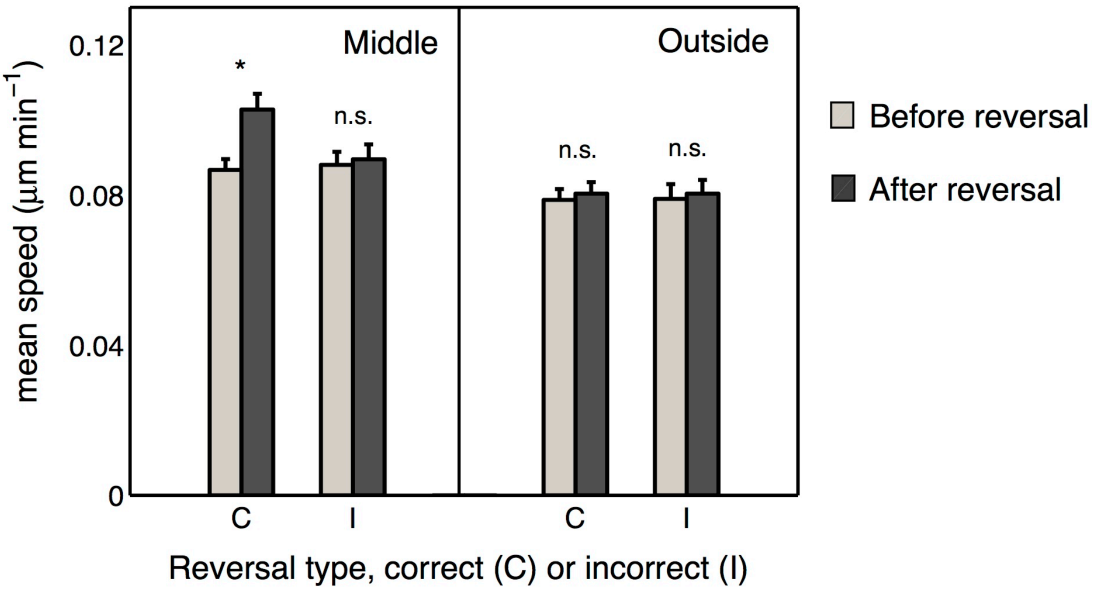

Fig. S12: Cells move faster after responding to a change in the direction of a chemoattractant gradient. We calculated the mean speed of individual cells before (light grey bars) and after (dark grey bars) they performed reversals (SI Materials and Methods), and pooled these according to whether they occurred in the "Middle" of the device (the region between the dashed lines in Fig. 4D,E), where spatial gradients are strongest, or on the "Outside" edges of the device (the region outside the dashed lines in Fig. 4D,E), where spatial gradients were relatively weak. Correct reversals occur in cells initially moving away from a chemoattractant source, and incorrect reversals occur in cells initially moving towards a chemoattractant source. Cells increase their speed after performing correct reversals in the middle of the channel, where they are induced at a higher rate (Fig. 4F). These asymmetries are not found in the outside region or for incorrect reversals. "n.s." denote non-significant differences in speed while "*" denotes a p-value < 0.05, according to paired-sample t-tests at a significance of 5%. Error bars are standard errors of means.

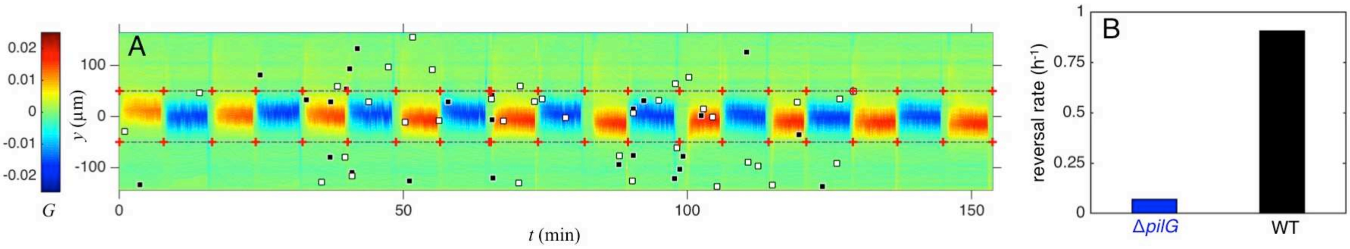

Fig. S13: Cells lacking the response regulator PilG cells rarely reverse direction in the alternating gradient experiment. (**A**) When Δ*pilG* cells were exposed chemoattractant conditions analogous to that shown in Fig. 4D, reversals (black and white boxes) occurred relatively infrequently when compared to the wild-type, which is consistent with the behavior of swimming Δ*cheY1* cells that rarely reverse their swimming direction and lack the ability to perform flagella-based chemotaxis (19). Data in A are presented in the same manner as Fig. 4D of the main text. (**B**) The reversal rate of Δ*pilG* and wild-type cells in the alternating gradient was quantified by dividing the total number of reversals (correct and incorrect) by the total time of trajectories (SI Materials and Methods), revealing that reversals occurred 13 times more frequently in the wild-type than in Δ*pilG*.

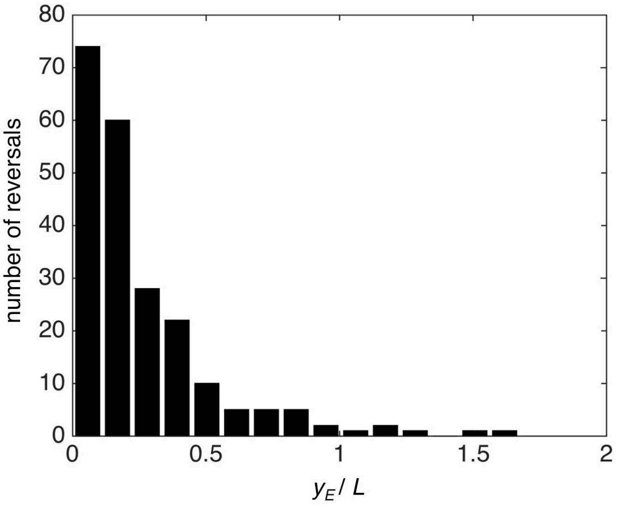

Fig. S14: Cells exposed to DMSO gradient that alternates direction respond quickly, typically reversing before they move a small fraction of their body length. Here we replot the data shown in Fig. 4G (inset), normalizing by the length of the cell body. After the gradient has changed direction, cells in our experiment move a distance, y_E, along the chemical gradient before they reverse to travel in the opposite direction. If cells sensed chemical gradients temporally, like swimming cells do (22), they would be able to measure the change in concentration over this distance. However, if cells measured gradients with a spatial mechanism, they would be able to measure the change in concentration over the entire length of their bodies, L. Thus, after the gradient has changed direction, a cell sensing in time would measure a change in concentration y_E / L smaller than a cell sensing in space. As in Fig. 4G (inset), the data shown here is for correct reversals in the middle of the device. Here y_E and L are the projections of cell movement and body length, respectively, along the gradient (i.e. in the y direction).

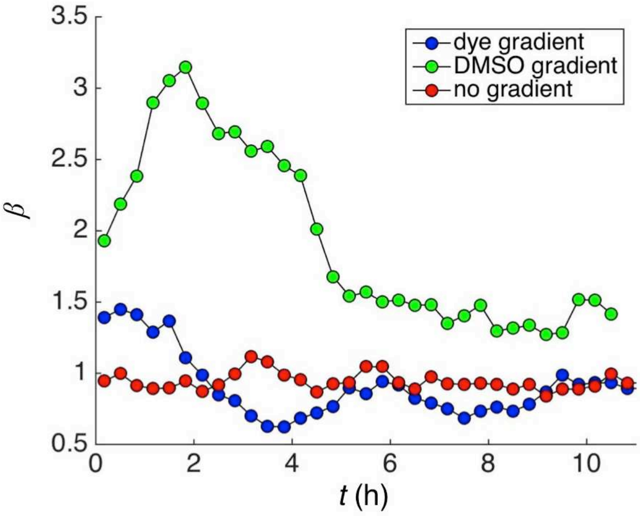

Fig. S15: Cells do not exhibit appreciable chemotaxis to Chicago Blue dye. The chemotactic bias, *β*, of cells in a gradient of dye (blue line) lacks the strong response observed in a gradient of DMSO (green line) and more closely resembles that of a gradient-free control (red line). We used this dye in alternating gradient experiments to track the distribution of chemoattractant within the microfluidic device.

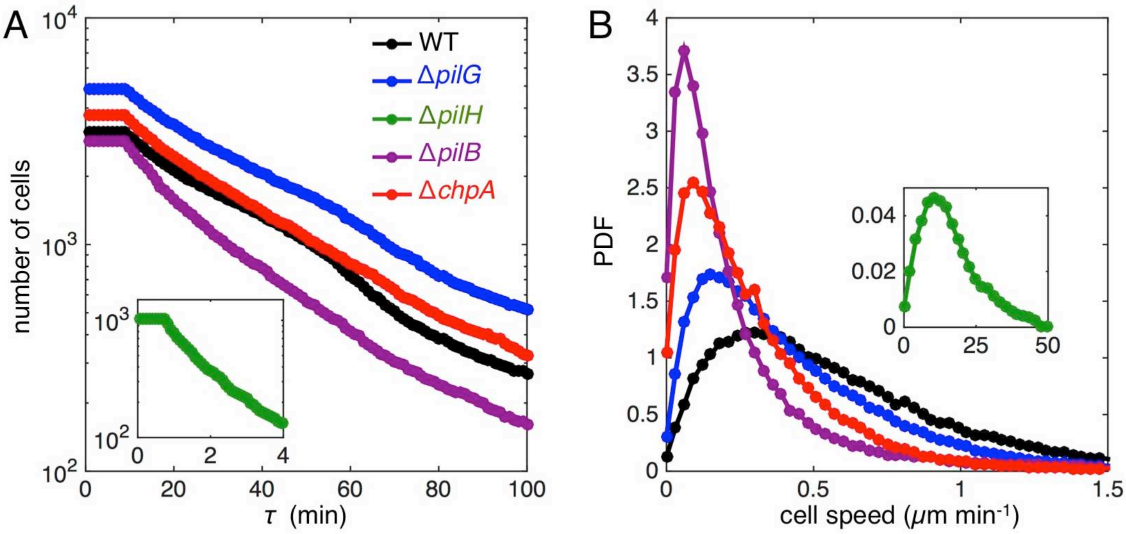

Figure S16: Quantification of the motility of Chp mutants. (A) In Fig. 3C we measure the root mean square displacement (RMSD) of cells in the absence of a chemical gradient to resolve the motility of different mutants of the Chp system. Here we show the number of cells from which these measurements were obtained. At small time lags, *τ*, RMSD is calculated from more than 1000 cells; whilst at the longest time lags are data is derived from more than 100 cell trajectories. To reduce the potential for spurious cell trajectories, we omit trajectories shorter than ten frames long from our analyses, which is responsible for the plateau observed at small *τ*. (B) The probability density function (PDF) of instantaneous cell speed shows the same trends as measurements of the RMSD (Fig. 3C). In both A and B, data for Δ*pilH* is shown in the insets. The axes of the insets are the same as the larger panel.

SI References

1. Bertrand JJ, West JT, & Engel JN (2010) Genetic Analysis of the Regulation of Type IV Pilus Function by the Chp Chemosensory System of Pseudomonas aeruginosa. *J Bacteriol* 192(4):994-1010.
2. Semmler ABT, Whitchurch CB, & Mattick JS (1999) A re-examination of twitching motility in Pseudomonas aeruginosa. *Microbiol-Sgm* 145:2863-2873.
3. Schindelin J*, et al.* (2012) Fiji: an open-source platform for biological-image analysis. *Nat Methods* 9(7):676-682.
4. Benoit MR, Conant CG, Ionescu-Zanetti C, Schwartz M, & Matin A (2010) New device for high-throughput viability screening of flow biofilms. *Appl Environ Microb* 76(13):4136-4142.
5. Haubert K, Drier T, & Beebe D (2006) PDMS bonding by means of a portable, low-cost corona system. *Lab Chip* 6(12):1548-1549.
6. Crank J (1975) *The mathematics of diffusion* (Clarendon Press, Oxford) 2nd Ed pp viii, 414 p.
7. Jaqaman K*, et al.* (2008) Robust single-particle tracking in live-cell time-lapse sequences. *Nat Methods* 5(8):695-702.
8. Ahmed T & Stocker R (2008) Experimental verification of the behavioral foundation of bacterial transport prameters using microfluidics. *Biophys J* 95(9):4481-4493.
9. Jin F, Conrad JC, Gibiansky ML, & Wong GCL (2011) Bacteria use type-IV pili to slingshot on surfaces. *P Natl Acad Sci USA* 108(31):12617-12622.
10. Seymour JR, Marcos, & Stocker R (2009) Resource patch formation and exploitation throughout the marine microbial food web. *Am Nat* 173(1):E15-E29.
11. Visser AW & Kiorboe T (2006) Plankton motility patterns and encounter rates. *Oecologia* 148(3):538-546.
12. Zhang Y, Ducret A, Shaevitz J, & Mignot T (2012) From individual cell motility to collective behaviors: insights from a prokaryote, *Myxococcus xanthus. FEMS microbiology reviews* 36(1):149-164.
13. Kearns DB & Shimkets LJ (1998) Chemotaxis in a gliding bacterium. *P Natl Acad Sci USA* 95(20):11957-11962.
14. Shi WY, Ngok FK, & Zusman DR (1996) Cell density regulates cellular reversal frequency in Myxococcus xanthus. *P Natl Acad Sci USA* 93(9):4142-4146.
15. Cowles KN & Gitai Z (2010) Surface association and the MreB cytoskeleton regulate pilus production, localization and function in Pseudomonas aeruginosa. *Mol Microbiol* 76(6):1411-1426.
16. Skerker JM & Berg HC (2001) Direct observation of extension and retraction of type IV pili. *Proc Natl Acad Sci U S A* 98(12):6901-6904.
17. Conrad JC*, et al.* (2011) Flagella and pili-mediated near-surface single-cell motility mechanisms in *P. aeruginosa*. *Biophys J* 100(7):1608-1616.
18. Kato J, Kim HE, Takiguchi N, Kuroda A, & Ohtake H (2008) P*seudomonas aeruginosa* as a model microorganism for investigation of chemotactic behaviors in ecosystem. *J Biosci Bioeng* 106(1):1-7.
19. Masduki A*, et al.* (1995) Isolation and Characterization of chemotaxis mutants and genes of *Pseudomonas aeruginosa. J Bacteriol* 177(4):948-952.
20. Sampedro I, Parales RE, Krell T, & Hill JE (2014) Pseudomonas chemotaxis. *FEMS microbiology reviews*.
21. Fulcher NB, Holliday PM, Klem E, Cann MJ, & Wolfgang MC (2010) The *Pseudomonas aeruginosa* Chp chemosensory system regulates intracellular cAMP levels by modulating adenylate cyclase activity. *Mol Microbiol* 76(4):889-904.
22. Berg HC (2004) *E. coli in motion* (Springer, New York).